The Astrophysical Journal, 894:148 (17pp), 2020 May 10 https://doi.org/10.3847/1538-4357/ab88cf

Modeling Observable Differences in Flare Loop Evolution due to Reconnection Location and Current Sheet Structure

John Unverferth and Dana Longcope
Department of Physics, Montana State University, Bozeman, MT 59717, USA
Received 2020 February 20; revised 2020 March 30; accepted 2020 April 3; published 2020 May 18

Abstract

Flare reconnection is expected to occur at some point within a large-scale coronal current sheet. The structure of the magnetic field outside this sheet is almost certain to affect the flare, especially its energy release. Different models for reconnection have invoked different structures for the current sheet's magnetic field and different locations for the reconnection electric field within it. Models invoking Petschek-type reconnection often use a uniform field. Others invoke a field bounded by two Y-points with a field strength maximum between them and propose this maximum as the site of the reconnection electric field. Still other models, such as the collapsing trap model, require that the field strength peak at or near the edge of the current sheet and propose that reconnection occurs above this peak. At present there is no agreement as to where reconnection might occur within a global current sheet. We study the post-reconnection dynamics under all these scenarios, seeking potentially observable differences between them. We find that reconnection occurring above the point of strongest field leads to the highest density and the highest emission measure of the hottest material. This scenario offers a possible explanation of superhot coronal sources seen in some flares.

Unified Astronomy Thesaurus concepts: Solar flares (1496); Solar magnetic reconnection (1504)

Supporting material: animations

1. Introduction

Fast magnetic reconnection is believed to occur within a small diffusion region localized inside a large-scale current sheet (Yokoyama & Shibata 1994; Erkaev et al. 2000; Biskamp & Schwarz 2001; Baty et al. 2006; Forbes et al. 2013). In spite of many theoretical investigations, there is not yet a consensus on the nature of the localized reconnection electric field or on the site within the sheet where it will occur. Small-scale modeling is often done within a current sheet separating uniform layers of magnetic field of equal magnitudes but different direction (Hesse et al. 1999; Birn et al. 2001; Karimabadi et al. 2004; Pritchett & Coroniti 2004; Shay et al. 2007; Drake et al. 2009; Landi et al. 2015). The external field strength is uniform along such a sheet, so the location of the reconnection site is irrelevant: all locations are equivalent. Such a uniform current sheet is the setting of standard Petschek models (Vasyliunas 1975; Soward 1982; Biernat et al. 1987; Forbes & Priest 1987).

A class of more realistic current sheets occur as tangential discontinuities in force-free magnetic fields (Priest & Raadu 1975; Aly & Amari 1989; Longcope & Forbes 2014). In two-dimensional versions, the current sheet terminates at a Y-type magnetic null point. The 2.5-dimensional relatives of these fields have a uniform magnetic field component in the ignorable direction, and only the other components vanish at the Y-point. In one well-known variety of this field, the Green–Syrovatskii field, the current sheet is terminated by Y-points at both ends and has a point of maximum field strength midway between them (Green 1965; Syrovatskiĭ 1971). In other cases, such as the illustration in Figure 1, the sheet may extend upward indefinitely, but with a peak field strength some finite distance above the Y-point.

In the more realistic geometries reconnection must be localized to some point, or small region, within the current sheet. As mentioned above, microscopic modeling has not yet reached a conclusion on where that point might be. There are, broadly speaking, three possibilities for its location, *viz.,* the Y-point and field strength maximum. Reconnection may occur precisely at the maximum, or it may occur on the side nearer to (below) or farther from (above) the Y-point. In every case, the newly reconnected field will be swept along the current sheet, away from the site of reconnection by reconnection outflows, driven by magnetic field line retraction. In the first two cases this retraction will move the flux into regions of the current sheet with weaker field. In the third case, reconnection above the peak, the retraction will move the flux toward the peak and therefore into a *stronger* field.

Different models of reconnection-powered solar flares have assumed reconnection in each of the possible locations. Modeling by Forbes et al. (2018) posited reconnection at the point of peak magnetic field strength. The surface current density of the sheet is maximum there, so in models where the reconnection electric field is directly related to current density, such as resistive MHD, the reconnection would occur there. Alternatively, models that invoke a collapsing trap assume that reconnection occurs above the point of peak field strength (Levine 1974; Somov & Kosugi 1997; Karlický & Kosugi 2004). The retracting field is then drawn into regions of increasing magnetic field strength, leading to particle acceleration by some variant of the betatron mechanism. Such a scenario implies a reconnection point above the field strength maximum. In models with a more complicated version of Ohm's law (i.e., generalized Ohm's law) the peak electric field need not coincide with the peak current density (Biskamp & Schwarz 2001; Bhattacharjee et al. 2009; Forbes et al. 2013). An example of this geometry is found in the model of the flare on 2017 September 10 by Longcope et al. (2018), which used EUV data to infer that reconnection-driven downflows were moving into increasing field strength.

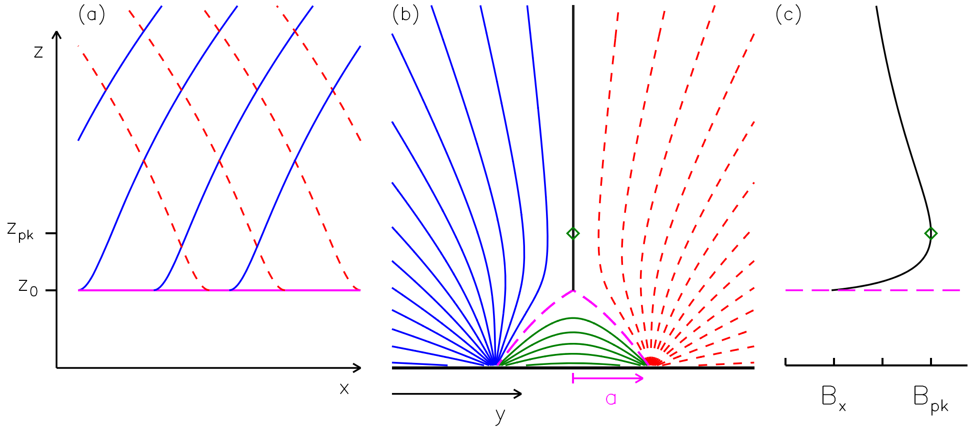

Figure 1. Illustration of the model field with a vertical current sheet above a single *Y*-point. (a) Field lines on the two sides of the current sheet, viewed face-on, in the *x*–*z* plane. Blue solid lines are upward field lines on the near side ($y < 0$), while red dashed lines are downward field lines on the far side ($y > 0$); due to the ignorable component $B_x > 0$, both field lines are directed rightward in this view. (b) Surrounding field lines in blue solid (upward), red dashed (downward), and green solid (closed). The black vertical line is the current sheet, and the magenta dashed curves are the separatrices below the *Y*-point. (c) Field strength, horizontally, vs. height. A green diamond marks the peak, at $z = z_{\rm pk}$, which matches the diamond in panel (b).

Theoretical modeling and direct observation have not yet provided definitive evidence of where the reconnection occurs within the current sheet. It is expected, however, that differing locations will lead to differing dynamics, and thereby differing observable consequences. For example, the temperature and density of the outflowing plasma will depend on the variation in confining magnetic field through which it moves. Retraction into a field of increasing strength will compress the flux, driving up its density. The present work will characterize these differences and their observable consequences by simulating retraction from different reconnection sites in a current sheet.

1.1. A Current Sheet Model

The full range of behaviors can be investigated using a single model equilibrium current sheet inspired by Longcope & Forbes (2014). The effects of different locations of the reconnection electric field are investigated by specifying different locations within the common model current sheet. We begin with a two-dimensional magnetic field, (y, z), due to two photospheric sources, $(y,\,z) = (\pm a,\,0)$, which is current-free except within a single, vertical current sheet along $y = 0$, $z > z_0$. The model field, taken from a modification of that in Longcope & Forbes (2014), is shown in Figure 1(b) and includes open upward and downward field lines, shown in blue and red, respectively, separated by a vertical current sheet (black line) extending indefinitely upward from a *Y*-point at $z = z_0$. The closed field lines below the *Y*-point, shown in green, form the magnetic arcade. It is surrounded by a separatrix linked to the *Y*-point, shown in magenta.

Just outside the current sheet (i.e., at $y = 0$) the vertical component of the magnetic field,

$$B_z(z) = \pm \frac{2B_0\sqrt{(z_0^2 + a^2)(z^2 - z_0^2)}}{z^2 + a^2}, \quad z \geqslant z_0, \qquad (1)$$

changes sign from upward (upper sign) on the $y < 0$ side to downward (lower sign) on the $y > 0$ side. In this expression B_0 is the peak of $|B_z|$, and a and z_0 are the locations of the sources and *Y*-point as described above. The dynamics of the retraction will be governed by the field strength just outside the sheet. Including an ignorable component, B_x, the field strength along the model current sheet is

$$B(z) = \sqrt{B_x^2 + B_z^2(z)} = \sqrt{B_x^2 + 4B_0^2\,\frac{(z_0^2 + a^2)(z^2 - z_0^2)}{(z^2 + a^2)^2}}, \quad z \geqslant z_0, \qquad (2)$$

plotted in Figure 1(c). The field assumes its minimum value at the *Y*-point, $B(z_0) = B_x$, that of the ignorable component alone. It achieves its maximum value, $B(z_{\rm pk}) = \sqrt{B_x^2 + B_0^2}$, at $z_{\rm pk} = \sqrt{a^2 + 2z_0^2}$, indicated by diamonds on Figures 1(b) and (c). It is evident from the edge-on view (Figure 1(b)) that field lines outside the current sheet (red and blue) curve inward toward the current sheet. These field lines most closely approach the current sheet at the field strength maximum, leading to it be sometimes called the *pinch point* (Forbes et al. 2018). This point serves as a marker for the strongest external field outside the current sheet.

We will consider scenarios where reconnection occurs at the pinch point and scenarios where it occurs elsewhere. As mentioned above, many models place the point of magnetic reconnection at the pinch point (Forbes et al. 2018). That location has the largest current surface density, so if the sheet thickness were uniform, it would have the highest current density. Under classical Ohm's law with uniform resistivity the electric field would be greatest there, making it the most likely point for reconnection. There are, however, many reconnection models in which the electric field is maintained by collisionless processes (Biskamp & Schwarz 2001; Bhattacharjee et al. 2009; Forbes et al. 2013), and reconnection may occur away from the point of peak surface current. For this reason we consider reconnection sites away from the pinch point.

We investigate the dynamics of magnetic energy release triggered by magnetic reconnection localized to some point within the model current sheet described above. We do this by specifying a point of magnetic reconnection, $z_{\rm rx} > z_0$. Fixing this to be the pinch point, $z_{\rm rx} = z_{\rm pk}$, provides the first scenario whereby a reconnected flux tube will move into ever weaker field and will therefore *expand* as it retracts; we hereafter call this the *expanding case*. Locating the reconnection site below the peak, $z_{\rm rx} < z_{\rm pk}$, would likewise lead to monotonic

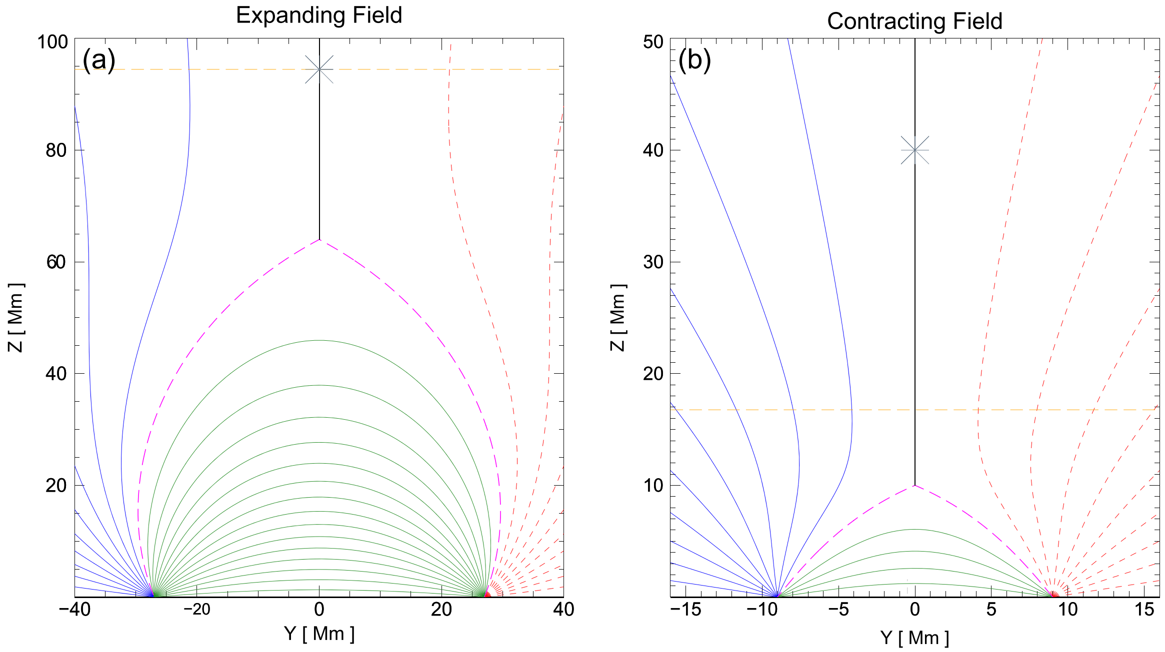

Figure 2. Current sheets used for the two case studies. In both panels, the magenta dashed line is a separatrix, splitting the field lines into three domains, and the solid black line marks the current sheet. The red dashed and blue solid lines are field lines that continue upward outside the upper bound of the simulation. The green solid lines are flux that has already reconnected and is closed off underneath the current sheet. The horizontal orange dashed line marks the peak magnetic field strength. The gray asterisk indicates the specified site of reconnection. (a) Expanding case, using $a = 27$ Mm and $z_0 = 64$ Mm. (b) Contracting case, using $a = 9.0$ Mm and $z_0 = 10.0$ Mm. $z_{\rm rx} - z_0 = 30$ Mm in both panels.

expansion following reconnecting. We therefore choose not to separately investigate this case. On the other hand, we expect a reconnection site *above* the peak, $z_{\rm rx} > z_{\rm pk}$, to yield qualitatively different behavior. In this case the tube will retract into increasing magnetic field, which will lead to a compression of the flux, so we hereafter call this the *contracting case*. Once the retracting tube passes the peak, it will begin expanding.

In addition to the reconnected flux retracting downward, there will be flux that retracts upward, perhaps forming an ejected flux rope. This is an equally important part of the reconnection scenario. In this work, however, we focus on that flux that constitutes the solar flare: the downward retracting flux. Hereafter we consider only that flux and use the terms "expanding" and "contracting" in reference to the evolution of the downward retracting flux.

To pursue this strategy, we choose values of a, z_0, and $z_{\rm rx}$ for the two distinct cases. We choose $z_{\rm rx} - z_0 = 30$ Mm in both cases, to give each the same distance to retract following reconnection. For the expanding case, we take $z_0 = 64$ Mm, $a = 27$ Mm, and $z_{\rm rx} = z_{\rm pk} = \sqrt{a^2 + 2z_0^2} = 94.45$ Mm, as shown in Figure 2(a). For the contracting case we choose, $z_0 = 10.0$ Mm, $a = 9.0$ Mm, and $z_{\rm rx} = 40.0$ Mm, as shown in Figure 2(b). The field strength peaks at $z_{\rm pk} - z_0 = 6.76$ Mm above the Y-point, so the first 77% of the retraction will be through increasing field. The two panels of Figure 2 are specific examples of the general field shown in Figure 1(b). Figure 2 is an edge-on view of the two current sheets used in this investigation. These are specific realizations of the general current sheet shown in Figure 1. (The edge-on views shown in Figures 1 and 2 are for context. Our model is entirely confined to the vertical current sheet—the x–z plane—so the y coordinate does not appear in it.)

We model the dynamics of flux following reconnection using the thin flux tube (TFT) approximation of MHD. First laid out for use in the convection zone and chromosphere by Spruit (1981) and later adapted for use in the corona in Linton & Longcope (2006) and Longcope et al. (2009), this model follows the retraction of a single tube of reconnected flux as it passes through the equilibrium current sheet. The model does not consider the process of reconnection, but rather it begins with the flux tube *just following* its reconnection at some location within the current sheet. The post-reconnection flux tube crosses from one side of the current sheet to the other, as shown in Figure 3. It follows an equilibrium field up one side, crosses the sheet at the specified reconnection point, $z_{\rm rx}$, and then proceeds down the other side. The otherwise force-balanced segments are thus joined together at $z_{\rm rx}$, with an angle

$$\Delta\theta \;=\; 2\,\mathrm{atan}\left[\frac{B_z(z_{\rm rx})}{B_x}\right] \tag{3}$$

between the two flux tubes—$B_z(z)(z_{\rm rx})$ is the function in Equation (1) evaluated at $z = z_{\rm rx}$. Letting $\Delta\theta = 180°$ would result in antiparallel reconnection without any guide field, and letting the angle approach 0° would result in no reconnection, as the field lines would be parallel.

The TFT assumes that the current sheet supplies the external pressure confining the retracting tube, but that the current sheet is not affected by the tube's motion. The confining field has a fixed spatial variation, $B(z)$, given by Equation (2). As retraction carries it through this varying field, the tube will experience a time-varying confinement pressure. A tube beginning where $B(z)$ is maximum, namely, $z_{\rm rx} = z_{\rm pk}$, will experience $dB/dt < 0$, leading to the designation of expanding. In the other case, beginning at $z_{\rm rx} > z_{\rm pk}$, the field strength will increase, $dB/dt > 0$, resulting in the tube's lateral contraction. To these two cases we add a third in which B is invariant along the sheet: $dB/dt = 0$. This represents the case of a uniform current sheet ($\partial B/\partial z = 0$), which has been most often used in

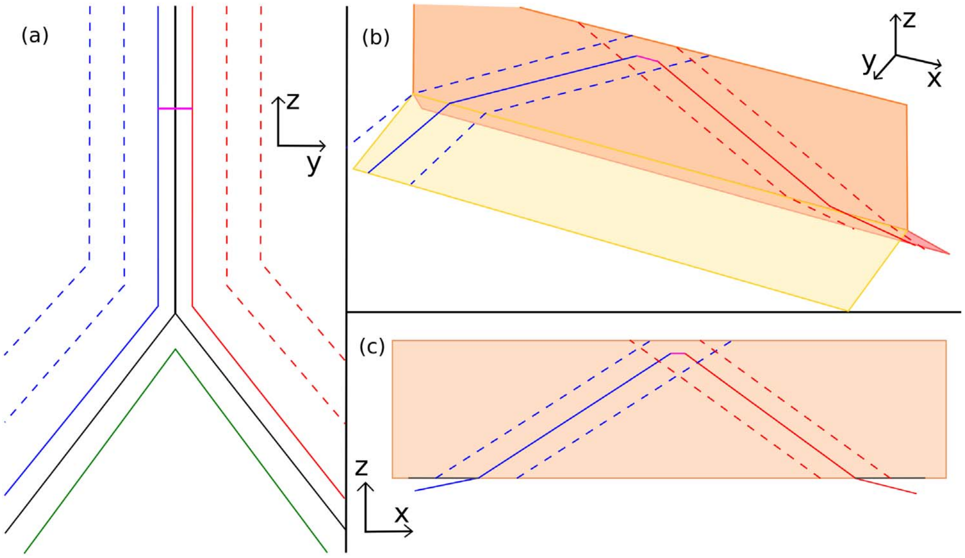

Figure 3. Schematic illustrating the field in three dimensions. (a) Simplified edge-on view of the magnetic fields seen before reconnection, with open flux shown in red and blue and closed flux shown in green separated by the solid black line. The solid red and blue are field lines that we force to reconnect with the magenta solid line. (b) Perspective view of the same sheet, rotated to show the extent of the field line. (c) Same field rotated solely into the x–z plane for a face-on view. The gray lines on the edge of the current sheet are the legs shown in blue and red after being moved to follow the current sheet edge.

past TFT simulations (Longcope et al. 2010, 2016; Longcope & Klimchuk 2015); we hereafter refer to this as the *uniform* case.

The present work uses the TFT model to explore how the different evolution resulting from different reconnection sites manifests in flares with observably different properties. To do this, we initialize the TFT with a flux tube of a given description and follow its evolution through a current sheet of the appropriate kind: uniform, expanding, or contracting. The evolution of each kind is characterized in terms of observable aspects such as peak temperature, peak density, and the full differential emission measure (DEM). Our analysis reveals that the expanding case reaches the greatest peak density and reaches this earlier than the other two cases. The other two cases, however, exhibit a high-temperature peak in their DEMs, absent from the expanding case.

The analysis is presented as follows. Section 2 introduces the TFT framework and uses it to investigate the three cases in depth. Section 3 follows the evolution of each case and provides a comparison of common evolutionary stages. Section 4 uses synthetic observables to compare the cases against one another.

2. The TFT Model

The TFT model incorporates reconnection-driven magnetic field evolution, more typically found in full MHD simulations, with the more efficient computation and ease of 1D flare loop models. The combination is achieved by representing the flux tube as a parameterized curve, moving through a static current sheet. Because only a single curve is represented, simulations can achieve the very high spatial resolution needed to accurately capture evolution of the transition region during a flare (MacNeice et al. 1984). While it considers transient evolution of only a single flux tube, the TFT model has been shown to match results of steady models in 2.5 dimensions (Longcope et al. 2010; Longcope & Klimchuk 2015) under comparable conditions. The TFT model does, however, ignore possible interactions between multiple flux tubes, or interactions of the tube with the surrounding field. Nevertheless, the model serves as an important preliminary step for investigating post-reconnection dynamics.

The present investigation solves the TFT equations using the Post-Reconnection Evolution of a Flux Tube (PREFT) code. First introduced in Longcope & Klimchuk (2015) and updated in Longcope et al. (2018), PREFT advances the TFT equations on a Lagrangian grid. The tube's axis, $\boldsymbol{r}(\ell, t)$, is represented by a chain of Lagrangian grid points whose length coordinates, ℓ, are continually recomputed. The evolution of the axis is specified by setting the Lagrangian derivative to the fluid velocity of that fluid element: $D\boldsymbol{r}/Dt = \boldsymbol{v}(\ell, t)$. The fluid velocity of each element (grid point) is advanced according to the momentum equation (Longcope & Klimchuk 2015; Longcope et al. 2018)

$$\frac{D\boldsymbol{v}}{Dt} = \frac{1}{\rho}\left(\frac{B^2}{4\pi} - p\right)\frac{\partial\hat{\boldsymbol{b}}}{\partial\ell} - \frac{1}{\rho}\frac{\partial p}{\partial\ell}\hat{\boldsymbol{b}} + \frac{B}{\rho}\frac{\partial}{\partial\ell} \times \left(\frac{\tilde{\eta}}{B}\hat{\boldsymbol{b}}\hat{\boldsymbol{b}}\cdot\frac{\partial\boldsymbol{v}}{\partial\ell}\right) + \frac{1}{\rho}\left(1 + \frac{4\pi p}{B^2}\right)\nabla_\perp\left(\frac{B^2}{8\pi}\right), \quad (4)$$

where p is the gas pressure, ρ is the mass density, and $\tilde{\eta}$ is the parallel component of the dynamic viscosity. The direction along the axis is given by the unit tangent vector $\hat{\boldsymbol{b}} = \partial\boldsymbol{r}/\partial\ell$.

The TFT model assumes that the tube's plasma β is sufficiently small that the field strength within the tube matches that of the static surrounding field, $B(z)$. The tube's axis is restricted to the vertical current sheet (i.e., the x–z plane), so the surrounding field strength is given by the function in Equation (2). A gradient in the external field strength exerts a force perpendicular to the tube's axis through the term in Equation (4) featuring $\nabla_\perp$. The mass density ρ is continually recomputed along with cell lengths, $\delta\ell$, in order to conserve the mass per unit flux in each cell: $\delta\ell\,\rho/B(z)$.

The right-hand side of the momentum equation, Equation (4), includes all the forces acting on an element of the flux tube. These contributions are magnetic tension partially offset by the internal gas pressure (first term), gas pressure gradient parallel to the tube (second term), and the divergence of the parallel component of the viscous stress tensor (third term). The dynamic viscosity, $\tilde{\eta}$, is computed using the classical, temperature-dependent Braginksii form (Braginskii 1965; Longcope & Klimchuk 2015), although we also require a minimum viscosity to ensure resolution. The final term, first introduced by Guidoni & Longcope (2011) and incorporated into PREFT by Longcope et al. (2018), accounts for the pressure exerted by a gradient in the confining field. Prior to that modification PREFT had considered only uniform current sheets in which this term would vanish.

The current sheet abuts closed magnetic field at its lowest edge, the Y-point. Downward retraction will be halted at this point by the upward magnetic pressure from closed flux below. We model this effect simply but crudely with an ad hoc force term resembling a damped spring; a similar approach was adopted by Guidoni & Longcope (2011). The ad hoc force,

$$\boldsymbol{F} = \hat{\boldsymbol{n}}[k(z - z_0) - d(\hat{\boldsymbol{n}} \cdot \boldsymbol{v})], \tag{5}$$

is added to the right-hand side of Equation (4) for any tube element whose vertical position $z < z_0$, the bottom of the current sheet. This expression uses the unit vector $\hat{\boldsymbol{n}} = \hat{\boldsymbol{y}} \times \hat{\boldsymbol{b}}$, which is orthogonal to the tangent vector and has a negative z component ($\hat{n}_z < 0$ since $\hat{b}_x > 0$ over the entire tube). When the tube is below the bottom of the current sheet, $z < z_0$, and the force becomes active, the first term in square brackets will be negative and will thus produce a force with an upward component—i.e., a restoring force. The second term, a Stokes-like drag, will always oppose the motion in a direction perpendicular to the axis. The two ad hoc constants, the spring constant k and the damping coefficient, d, are set through preliminary experimentation to minimize the bounce-back of the tube and stop its retraction in approximately one oscillation.

The temperature of the tube is advanced according to the energy equation

$$\tilde{c}_v \frac{DT}{Dt} = -T(\nabla \cdot \boldsymbol{v}) + \frac{\bar{m}}{k_{\rm B}} \frac{\tilde{\eta}}{\rho} \left(\hat{\boldsymbol{b}} \cdot \frac{\partial \boldsymbol{v}}{\partial \ell} \right)^2 + \frac{\bar{m}}{k_{\rm B}} \frac{B}{\rho} \frac{\partial}{\partial \ell} \left(\frac{\kappa}{B} \frac{\partial T}{\partial \ell} \right) + n_e^2 \Lambda(T) + Q(\ell) \ , \tag{6}$$

where $\tilde{c}_v$ is the volumetric specific heat, T is the temperature, $\bar{m}$ is the mean particle mass, κ is the thermal conductivity, $\Lambda(T)$ is the radiative loss function, n_e is the electron number density, and Q is some heating applied to the tube. The first term on the right-hand side is the adiabatic change in temperature due to the expansion or contraction of the plasma. The second term is the viscous heating, and the third term is thermal conduction. PREFT uses a classical Spitzer conductivity subject to a limiter to satisfy the free-streaming limit (Longcope & Klimchuk 2015). Using a nonuniform magnetic field requires that account be taken of the varying cross-sectional area, inversely proportional to field strength B, in all divergences. The fourth term in Equation (6) is the radiative loss function for optically thin losses, and the final term is equilibrium heating applied to the flux tube.

PREFT advances these equations through a second-order time scheme, whose time steps are governed by the Courant–Friedrichs–Lewy conditions to ensure stability. Thermal conduction alone is advanced implicitly, so this extremely stringent time-step constraint can be neglected. The endpoints of the tube are fixed in both position and temperature, resulting in closed boundaries for both equations.

2.1. Initial Conditions

Equations (4) and (6) are solved beginning with an initial condition representing the loop just following its creation by reconnection across the current sheet. The post-reconnection form is an axis like that shown in Figure 3, which we create in two steps. In the first step a flux tube of the desired initial length is placed in a uniform magnetic field. Temperature is initialized by assuming constant pressure and solving for an equilibrium balancing classical thermal conduction and radiative losses against uniform volumetric heating Q (a so-called RTV equilibrium; Rosner et al. 1978). The pressure and heating rate are fixed to achieve a specified apex temperature for the prescribed half-length. After assuming uniform pressure, the solution is independent of axis geometry. This first step uses uniform cross section (i.e., uniform B) in the conduction term; the next step adjusts the heat flux $Q(\ell)$ to accommodate the actual cross-section variation.

In the second step, we compute the axis of the initial flux tube. Starting at the point of reconnection, $z_{\rm rx}$, we integrate a field line by solving $dz/dx = B_z(z)/B_x$, with $B_z(z)$ taken from the lower sign of Equation (2). The integration ends when the field line reaches the bottom edge of the current sheet, $z = z_0$. This will occur *before* reaching the half-length specified in the first step. The extra length represents the lower leg of the tube, which would follow the separatrix above the arcade, as shown in Figure 3. To simplify our modeling, we replace this complicated, nonplanar shape with a horizontal straight leg extending along $z = z_0$, to the half-length specified in the first step. This modification is illustrated in Figure 3(c). The field strength along this straight segment is therefore uniform, $B = B_x$.

Finally, the foot of this leg is given a 3 Mm stratified chromosphere. This highly simplified layer is meant to provide a source for evaporated material. This region alone is subject to a gravitational force, which is directed parallel to the leg. By taking it to be isothermal, $T = 30{,}000$ K, and free of heating or radiative losses, the layer will have exponential density and pressure profiles. In spite of its low temperature, it is assumed to be fully ionized at all times, and subject only to optically thin radiative losses (Longcope 2014) when heated.

Having completed the right side of the post-reconnection field line, we reflect it to form the left side, resulting in a symmetric flux tube. Finally, to ensure that the apex of the flux tube is adequately resolved, we round off the corner where the left and right halves join. This bend represents the result of localized reconnection that made the connection through the current sheet. Once the tube is set in place, we recalculate the magnetic field along the tube based on its new position in the current sheet in Equation (2). It is at this point that the volumetric heating, Q, is recomputed to yield a static solution to the energy Equation (6).

The above procedure is followed for each of the three different flux tubes, using the appropriate version of Equation (2) in each case. Since each flux tube has the same length and the same peak temperature, our procedure gives each case the same initial density profile. The cases are therefore well suited for comparison. One small difference comes from the larger magnetic field strength we choose for the uniform case. This means that its flux tube has less volume and

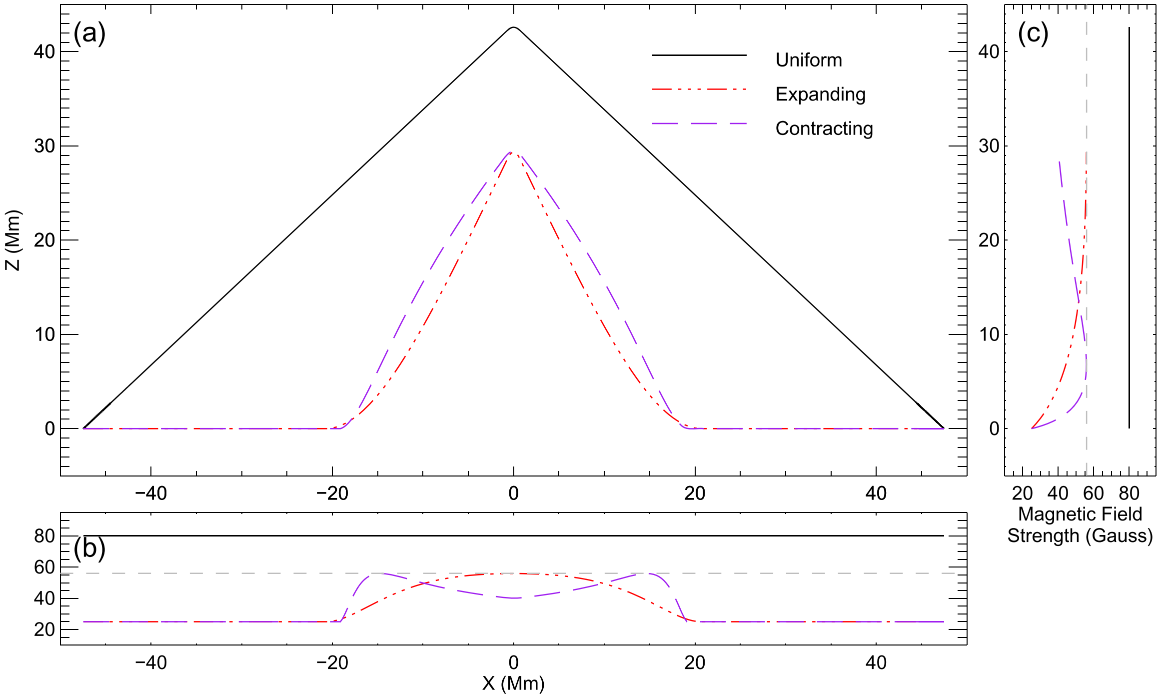

Figure 4. Initial configuration of the flux tube. (a) Spatial configuration in the face-on view. (b) Magnetic field as a function of x matching the horizontal coordinate from panel (a). (c) Field strength horizontally vs. the vertical z coordinate matching panel (a). In each panel there are three cases: uniform, expanding, and contracting, indicated by the solid black, dashed–dotted red, and dashed purple lines, respectively.

therefore less mass per flux than the expanding or contracting cases.

The field line shape found in the second step by solving $dz/dx = B_z(z)/B_x$ is only an equilibrium solution of the momentum equation, Equation (4), in the limit $\beta = 0$. While a finite β could be accommodated using a different integration method, the values of β in the corona are low enough that we use the simpler method described above. In addition, these flux tubes are unlikely to be in an exact equilibrium, as they have just undergone reconnection.

The initial conditions for the three cases are shown in Figure 4. Panel (a) shows spatial configuration within the current sheet (the x–z plane) from a face-on view. Each shape is a result of the relative strengths of the guide field to the current sheet field. Since these components do not vary in the uniform case, its legs are straight. In contrast, the expanding case flares out toward the bottom where the guide field begins to dominate. The contracting case bows inward and then flares out. In each of these cases, the overall starting length is the same to within 700 km. The apparent discrepancy in length between the uniform and nonuniform cases arises from the different angles at which they leave the base of the current sheet. The uniform case also reaches higher up into the current sheet. The current sheet in the uniform case is a constant strength, and this additional height was used to keep the internal properties of the tube, along with the initial and final lengths consistent with the other cases.

Panel (b) of Figure 4 shows the magnetic field strength as a function of z. With this perspective it is clear that the expanding case will encounter ever-weakening magnetic field during its retraction. In contrast, the contracting case will move first through increasing field before reaching the weakening field down to the edge of the current sheet. Panel (c) shows the magnetic field as a function of x. The extent of the weak magnetic field in the middle of the flux tube is clear. This is the amount of the flux tube that must undergo contraction before expansion.

The plasma properties in each case are chosen to be as similar as possible in order to focus our study on the effects of differing magnetic environments. Figure 5 shows the initial state of the uniform case using a format with which evolution will be plotted in the upcoming section. Panel (a) repeats the configuration from Figure 4(a) for the uniform case alone. Panels (b) and (c) show the electron number density and pressure, respectively, from the left chromospheric footpoint to the corona, just past the midpoint. The coronal part of the flux tube has uniform pressure, as described above. The footpoint regions are isothermal and gravitationally stratified. Panel (e) shows the temperature. With a fixed minimum value in the chromosphere, the temperature then quickly rises to peak at the specified value of 3 MK at the apex.

3. Time Evolution of the Three Cases

The post-reconnection evolution is obtained by solving the TFT Equations (4) and (6) beginning at $t = 0$ with each of the initial conditions in turn. The evolutions of the three cases share many common features and differ in several important respects. Their initial conditions and subsequent evolution are compared in Table 1. The cases have been designed to be similar in key respects evident from the table. These include their total lengths before and after retraction (128 and 95 Mm, respectively) and the total magnetic energy released: roughly 2×10^{10} erg Mx^{-1} in every case. Differences between the runs result from the differing current sheets through which they retract. The differences are most readily understood by comparing common evolutionary moments. These moments are best illustrated using the run with uniform field, which serves as a kind of base case.

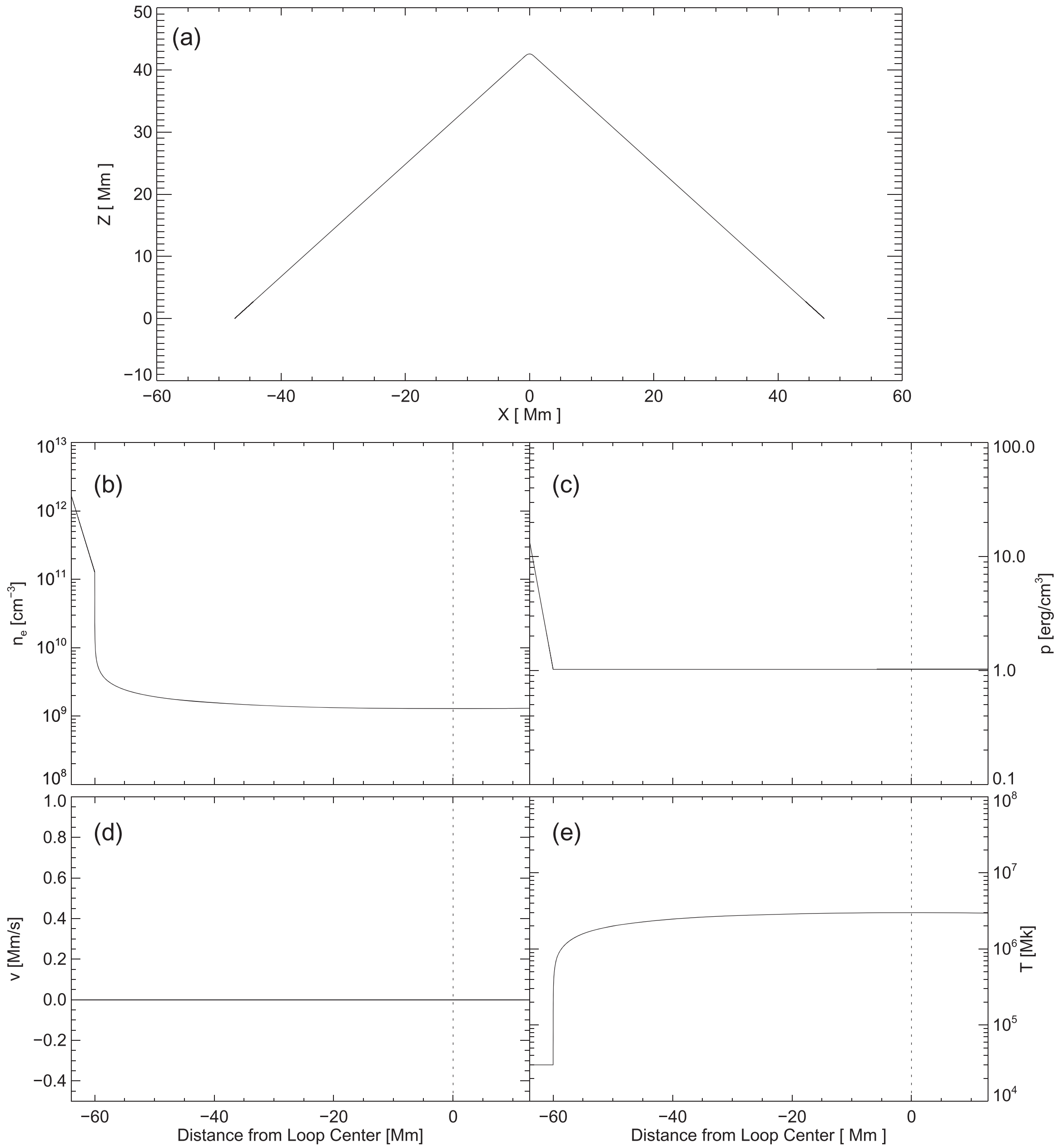

Figure 5. Initial conditions for the uniform case. (a) Flux tube's position in space. (b) Electron density as a function of tube length, zeroed at the center. (c) Pressure. (d) Velocity along the tube. (e) Temperature.

3.1. Evolution in a Uniform Field

The time evolution of the uniform case is shown at key evolutionary moments in Figure 6 using a format matching the equilibrium plots of Figure 5 (an animation is also available). The first event of note is the formation of retraction-powered jets evident at 1 s, shown as blue solid lines in each panel. These jets are powered by the rotational discontinuities (RDs) at either of the bends moving down the legs (Longcope et al. 2009), evident in panel (a). They begin to form immediately and are well developed by 1 s. The flow is accelerated by the magnetic tension at the two bends. As the simulation advances, the jets reach a steady velocity in excess of 1 Mm s^{-1}. The mass that they move into the center of the tube creates a large increase of density there, as the material shocks when it collides with the counterpart jet from the other side. This shock is responsible for compression and bulk heating of the plasma. In this TFT model, the viscosity is responsible for converting the bulk kinetic energy to thermal energy.

Thermal conduction carries heat from the center of the tube outward, until it reaches the chromosphere. Thermal conduction is close to the free-streaming limit, bringing the flux limiter into play and producing the very steep fronts evident in the blue solid line (1 s) of Figure 6(e). The conduction front reaches the chromosphere at $t = 14.3$ shown by green dashed–dotted lines. Since the plot uses a length coordinate with zero at the midpoint, the left boundary appears to move inward as the length decreases during retraction. As the flux tube continues to retract, the plasma jets continue to turn bulk motion into heat. Thermal conduction moves this heat down to the footpoints of the loop swiftly. As time advances from $t = 1.0$ to 14.3, the front moves outward, and it retains this sharp form until reaching the chromosphere. When the conduction front reaches

Table 1
Collection of Initial Conditions and Summarized Results for Each Case

	Uniform	Expanding	Contracting
T_{min} (MK)	0.03	0.03	0.03
T_{max} (MK)	3.0	3.0	3.0
Min n_e (log10(cm^{-3}))	9.1	9.1	9.1
Peak magnetic field strength (G)	80	55.9	55.9
$\Delta\theta_{\mathrm{rx}}$—the field angle at reconnection site	$84\overset{\circ}{.}2$	$126\overset{\circ}{.}8$	$103\overset{\circ}{.}6$
Maximum initial plasma β	0.002	0.021	0.021
Maximum plasma β	0.621	3.38	1.07
Initial length (Mm)	127.9	127.2	127.5
Final length (Mm)	94.9	94.9	94.9
Total energy loss (10^8 erg Mx^{-1})	164.64	158.28	164.22
Magnetic energy loss (10^8 erg Mx^{-1})	205.26	195.33	192.72
Peak temperature (Mm)	25.17	33.61	22.77
Time of peak temperature (s)	0.3	1.8	14.7
Time to hit bottom (s)	14.3 (center)	10.4 (center)	13.0 (sides)
The middle right time to finish retraction (s)	27.4 (1% of final length)	12.5 (sides)	15.1 (center)

the cooler dense material in the chromosphere, it heats the plasma there, driving a sharp increase in the pressure. This pressure spike drives the material to expand marking the beginning of evaporation.

At the same time, $t = 14.3$ s, the flux tube reaches the edge of the current sheet, activating the restoring force placed at $z = z_0$. The center of the tube reaches the edge first as a result of being launched downward with the local Alfvén speed from the tube's apex. The initial condition of the tube is such that the apex has the lowest density and thus has the highest Alfvén velocity. This means that the center will move down faster than any portion of the tube and will reach the edge first. In this run the center reaches the current sheet edge at virtually the same time that the conduction front reaches the chromosphere. As the flux tube encounters the edge of the current sheet, it is then slowed by the underlying spring force. While this force attempts to remove the perpendicular velocity with minimal impact on the tube's internal dynamics, it does create some secondary viscous heating effects.

After being heated, the chromospheric plasma begins to evaporate and condense. Figure 6 shows the flux tube at 20 s in yellow solid lines and then at 30 s in red dashed lines. The increase in pressure in the chromosphere that was mentioned above forces the plasma outward both to the center and to the foot. In this run, the initial evaporation is a slight pulse that occurs shortly after the conduction front arrives. This pulse can be seen in Figure 6 in panel (b) for density. This pulse clears out the flux tube, leaving a relative rarefaction behind it as it moves to the center. As more plasma becomes heated in the dense regions, conditions become favorable again for steady evaporation to begin. At 30 s, steady evaporation can be seen in the red lines in Figure 6. The pulse can also be seen, having damped out somewhat, and followed by the steady state closer to the foot of the flux tube.

3.2. Evolution of the Expanding Case

The nonuniform magnetic field of the expanding case leads to evolution, shown at key times in Figure 7, differing in several respects from the uniform case. The blue solid lines show the flux tube at 1 s when the jets powered by the RDs work to pile material into the center of the flux tube. As before, the compression and shocks there heat the central material. The peak temperature depends on the parallel flow from the jets, which in turn depends on the local Alfvén speed, v_{A}, and the angle between the reconnecting field, $\Delta\theta_{\mathrm{rx}}$, as $v_{\|} = 2v_{\mathrm{A}} \sin^2(\Delta\theta_{\mathrm{rx}}/4)$ (Longcope et al. 2009). The expanding case has smaller field strength at the reconnection point ($B_0 = 56$ vs. 80 G), and thus a lower Alfvén speed there. The magnetic field angle at the reconnection point is, however, much greater in the expanding case, $\Delta\theta_{\mathrm{rx}} = 127^\circ$ versus 84°, leading to faster jets (see Figure 7(d)) and consequently higher peak temperature (34 MK vs. 25 MK) as shown in Figure 7(e). This higher temperature drives the conduction fronts faster, so by 8.1 s, shown by the green dashed–dotted line, they have reached the chromosphere, while the tube is still retracting. The slower fronts of the uniform case reached the chromosphere at roughly the same time the tube reached the end of the current sheet.

The tube's encounter with the current sheet bottom, shown at 10.4 s in solid yellow, is similar to the encounter observed in the uniform case. The tube's midpoint was accelerated to the local vertical component of the Alfvén speed, which, as in the uniform case, is the largest at the midpoint. The initial downward velocity, $v_z = -v_{\mathrm{A}} \sin(\Delta\theta_{\mathrm{rx}}/2)$ (Longcope et al. 2009), is comparable in the two cases, as their differing values of v_{A} and $\Delta\theta_{\mathrm{rx}}$ tend to offset one another. Reconnection occurs lower in the expanding case (see Figure 4(a)), so the midpoint reaches the bottom slightly earlier than in the uniform case (10.4 s vs. 14.3 s). From the initial contact at the midpoint, the tube's encounter with the bottom spreads outward as it did in the uniform case.

3.3. Evolution of the Contracting Case

The nonuniform field of the contracting case leads to evolution different from both the uniform and the contracting cases, evident in the key times shown in Figure 8. The jets have once again begun by 1 s (blue dashed lines) but are much weaker than in the other cases. This is a result of reconnection at a point of low field strength and thus low Alfvén speed. The weaker jets produce a lower central temperature, at least initially. The thermal conduction from this cooler center does not approach the free-streaming limit, so the heat fronts are shallower than in the other two cases. The conduction front also moves more slowly, so it has not yet reached the chromosphere when the retraction reaches the current sheet edge at 13 s (green dashed–dotted lines).

The retracting tube of the contracting case encounters the bottom of the current sheet in a manner entirely different from the encounter of the other two cases. The RDs move at the local Alfvén speed, which increases downward in the contracting case. The outer corners therefore move downward faster than the middle, making the retracting segment concave downward, as clear from the green curve in Figure 8(a). The corners (i.e., the RDs) therefore reach the base of the current sheet ahead of the midpoint. The midpoint hits the bottom last, and the thermal conduction front reaches the chromosphere shortly afterward, at 16.3 s and shown in solid yellow. The last event shown is at 30 s and in red dashed lines, and like the previous cases, it highlights the development of steady evaporation. As a

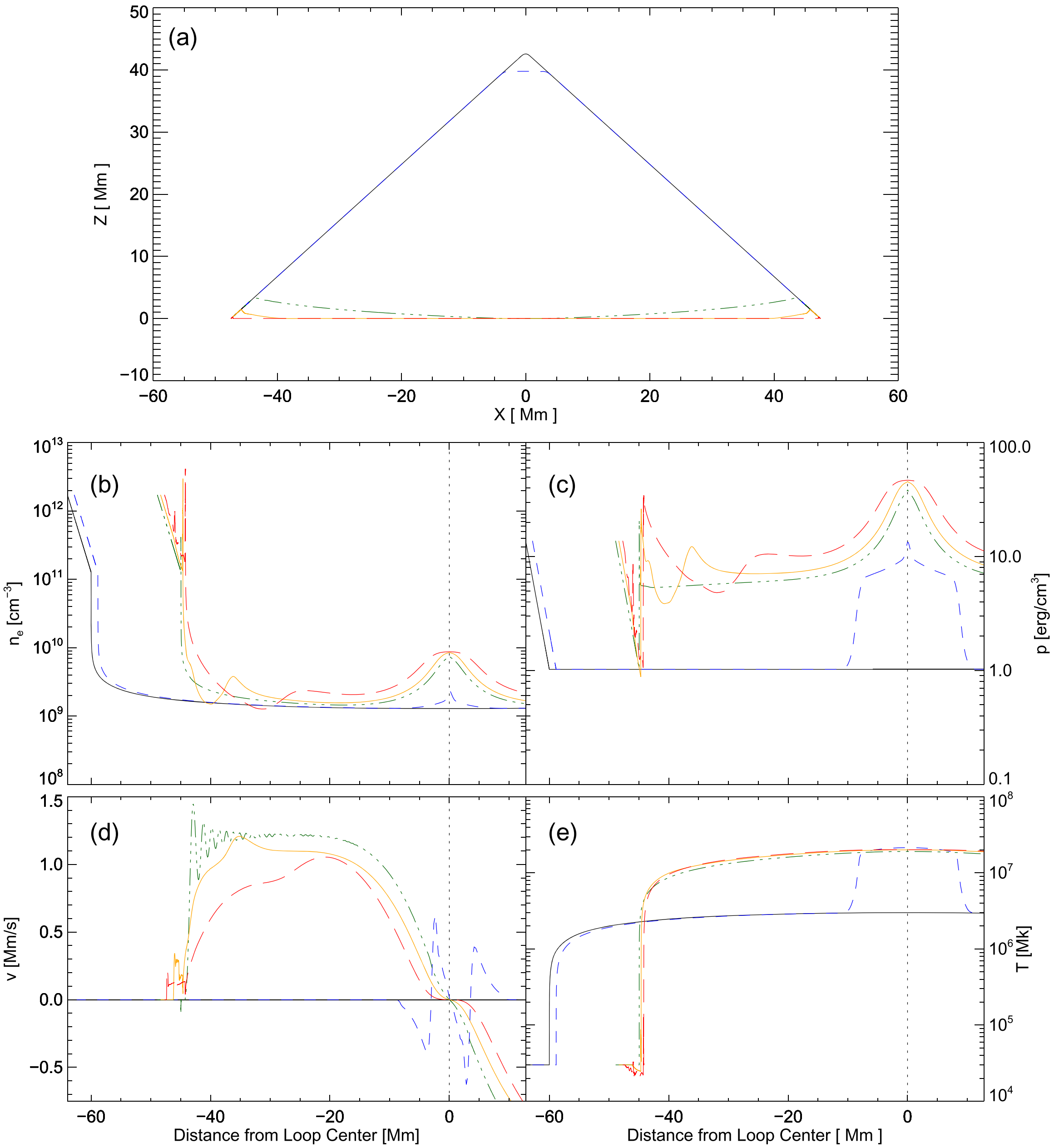

Figure 6. Evolution of the uniform case. (a) Flux tube's position in space. (b) Electron density as a function of tube length, zeroed at the center. (c) Pressure. (d) Velocity along the tube. (e) Temperature. In each panel the color corresponds with the time; black solid is 0 s, blue dashed is 1.0 s, green dashed–dotted is 14.3 s, yellow solid is 20.0 s, and red dashed is 30.0 s. An animation is available. The video shows the entire 30 s sequence.

(An animation of this figure is available.)

result of starting in the weakest field, this case seems to be the weakest in these time steps.

4. Run Results and Analysis

4.1. Energy Evolution

Global properties of the runs, such as their energy evolution shown in Figure 9, have common elements but also differ in key respects. To more clearly show gains and losses, the plot shows the energies less their initial value. Different colors show different forms of energy, namely, total energy (black), magnetic energy (violet), thermal energy (red), total kinetic energy (dark green), and that portion of the kinetic energy directed along the flux tube (light green). All energies are calculated per unit flux (i.e., erg Mx^{-1}) but can be multiplied by the flux of a single tube, or an entire flare, to obtain a more familiar value in erg.

Each case shows an immediate drop in magnetic energy accompanied by a matching gain in total kinetic energy. Magnetic tension works to pull a flux tube down to the bottom of the current sheet. In the uniform case that is the only force acting on the flux tube. For the expanding case, the tube is also being squeezed out of the region of high field by the magnetic pressure term—the final term in Equation (4). For the contracting case, this pressure works against the retraction as it moves into higher field regions. The result of this is that in the expanding case, the magnetic pressure and tension work in the same direction, speeding up the retraction process, while

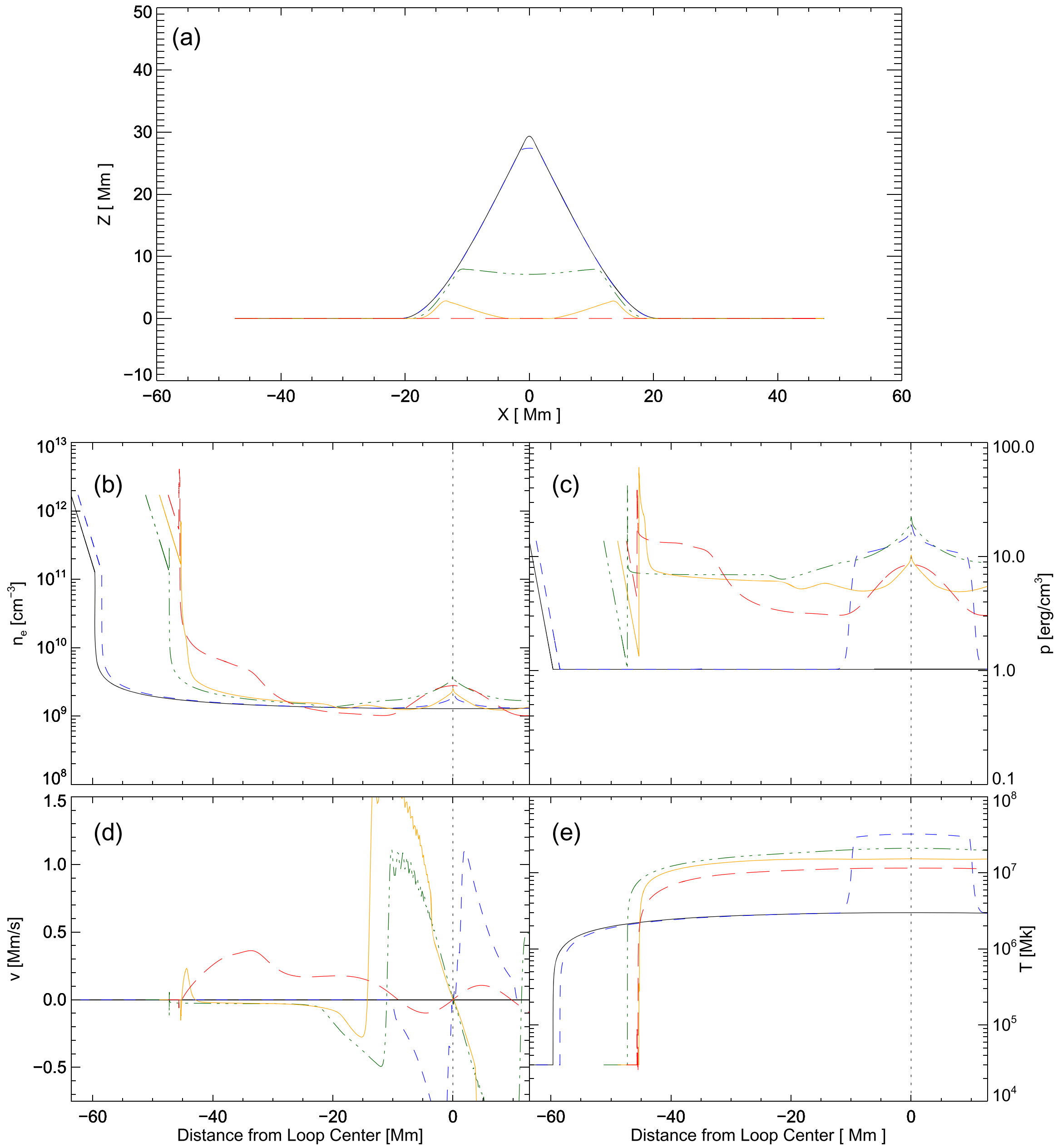

Figure 7. Evolution of the expanding case. (a) Flux tube's position in space. (b) Electron density as a function of tube length, zeroed at the center. (c) Pressure. (d) Velocity along the tube. (e) Temperature. In each panel the color corresponds to the time; black solid is 0 s, blue dashed is 1.0 s, green dashed–dotted is 8.1 s, yellow solid is 10.4 s, and red dashed is 30.0 s. An animation is available. The video shows the entire 30 s sequence.

(An animation of this figure is available.)

in the contracting case the pressure partly offset the tension, slowing the retraction.

While most of the kinetic energy in each simulation is in motion perpendicular to the axis, a smaller fraction is in flows directed along the tube. The latter portion is the energy of the parallel jets responsible for the majority of the heating, ultimately leading to the increase in overall thermal energy.

The instant the flux tube reaches the edge of the current sheet appears as the sharp drop in both total energy and the total kinetic energy. At this instant the ad hoc force comes into play, doing negative external work on the tube and decreasing its energy. Since this force takes the place of upward force from the underlying arcade, the energy would in reality go into its compression, possibly radiating as fast magnetosonic waves. In any event, the energy does not remain on the flux tube. The parallel motions will, however, remain on the tube and are unlikely to couple strongly to the compressive, perpendicular motions. In the uniform case, in particular, the parallel kinetic energy (light green) shows little effect from the damped spring at the end of retraction.

Each run shows similar features, though the magnitude and timing of these features differ between the cases. While the uniform case reaches higher temperatures than the contracting case, it has less mass (per unit flux) to heat, so its thermal energy (per flux) remains lower. The same effect results in the other two runs losing their thermal energy near the end of the simulation as the extra mass leads to more effective radiation,

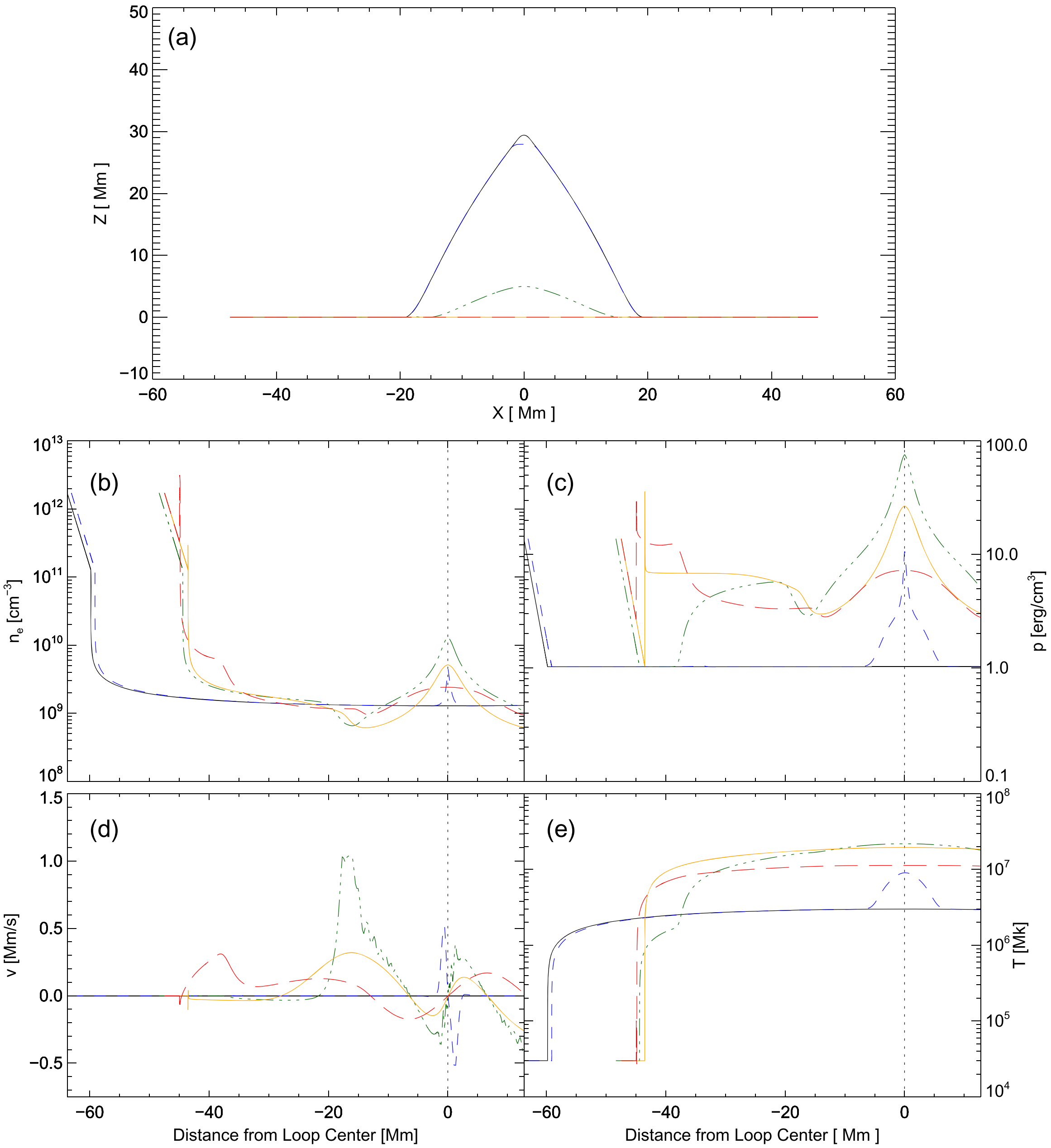

Figure 8. Evolution of the contracting case. (a) Flux tube's position in space. (b) Electron density as a function of tube length, zeroed at the center. (c) Pressure. (d) Velocity along the tube. (e) Temperature. In each panel the color corresponds to the time; black solid is 0.0 s, blue dashed is 1.0 s, green dashed–dotted is 13.0 s, yellow solid is 16.3 s, and red dashed is 30.0 s. An animation is available. The video shows the entire 30 s sequence.

(An animation of this figure is available.)

allowing them to cool more rapidly. Finally, the uniform and expanding cases have a steep initial drop in the total and kinetic energies followed by a slower loss. In contrast, the contracting case initially loses both slowly and then experiences a steep loss at the end. The difference is a result of the flux tube hitting the edge of the current sheet with the middle first in the first two and the corners first for the contracting case. The results of Figure 9 further confirm the similar characteristics of the runs noted before in Table 1.

4.2. Comparison of Observables

Several key differences between the cases are evident when temperature is plotted versus both space and time as a stack, shown in Figure 10. These were created by taking the temperature as a function of length along each loop, using the midpoint as zero. Each successive time step is appended to create a two-dimensional map of the temperature, using color, versus both space (vertically) and time (horizontally). In each of the three panels the thermal conduction front appears as a red wedge with a vertex at the time and place of reconnection: $(t, \ell) = (0, 0)$. The green region below this wedge is the 3 MK coronal plasma of the initial loop. Below this is a black wedge along the lower axis and whose upper edge is the left boundary of the simulation. The boundary point is fixed in space but appears to move in the stack plot as an artifact of our using integrated length as the spatial coordinate. The tube's retraction decreases the length separating the midpoint, $\ell = 0$, from the

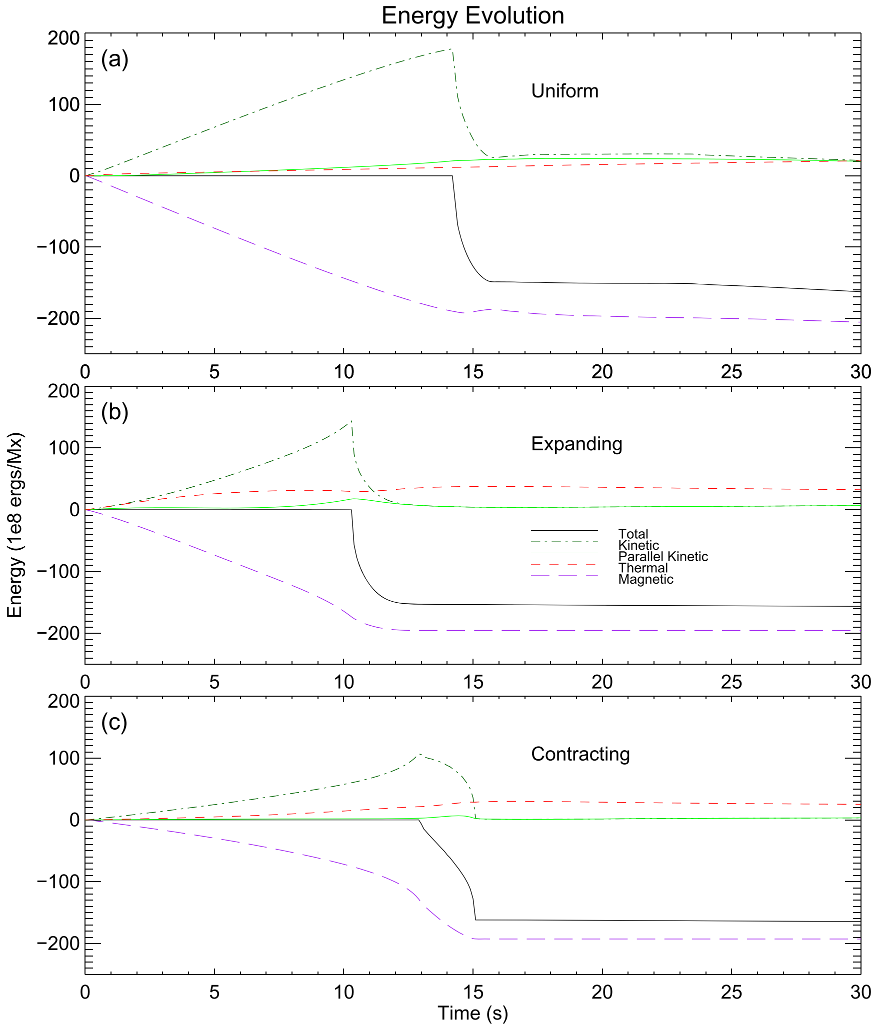

Figure 9. Time history of various energies in units of 10^8 erg Mx^{-1}, for (a) the uniform case, (b) the expanding case, and (c) the contracting case. In each panel the energies have been offset by their initial values to clearly show gain and loss. Solid black is the total energy, red dashed the thermal, dark green dashed–dotted the total kinetic, solid light green the parallel kinetic, and violet dashed the magnetic energy.

fixed boundary point. This has the effect of changing the length coordinate at which this stationary boundary appears.

There are notable differences in the temperature evolutions of the three cases. In the uniform case, the highest temperature is created very quickly, 0.3 s into the simulation, as shown by the change from green to red along the upper horizontal $\ell = 0$ line in Figure 10(a); this represents temperature increasing from the starting 3 MK to just over 25 MK. This case has the most uniform rate of magnetic energy release, and as such the most uniform conversion of that released energy into kinetic and thermal forms. For that relatively constant rate, the most effective temperature increase is the beginning, when the plasma in the middle of the flux tube is still rarefied. Thereafter the peak temperature drops steadily. This contrasts with the expanding case that reaches its maximum temperature 1.8 s after it begins retracting. The color table saturates at $T = 10^{7.5} = 32$ MK, so the peak appears here as a white region in panel (b). The expanding case retracts from the strongest field at the beginning of the simulation. This allows for a high rate of conversion from magnetic to kinetic energy compared with later times. With more mass in the tube, the overall partition of kinetic energy is smaller. More of that kinetic energy was directed along the tube in the early time of the run, allowing for stronger interactions between the jets, resulting in a higher temperature.

Both of these differ radically from the temperature evolution of the contracting case shown in Figure 10(c). With the retraction starting in a low field strength, the contacting case cannot build strong jets to start with. This results in a relatively cool loop top and a slow conduction front evident from the shallower slope of that front in Figure 10(c). When the retraction does reach strong field regions and can begin to generate more heat, the central region of the flux tube has been insulated from cooler coronal plasma by the initial smaller heat generation. While the peak temperature in this case is lower, there is, due to this insulating effect, still a high-temperature central component that would otherwise have been diminished by spreading throughout the full loop length. As a result, we can clearly say that the temperature evolution in each case has been clearly influenced by the current sheet profile.

Retracting through different field profiles results in a dramatically different evolution of the central density. Density stack plots for the three runs displayed in Figure 11 are constructed in the same manner as the temperature stack plots of Figure 10. These show the same black wedge along the left boundary, but no signature of the conduction fronts since those

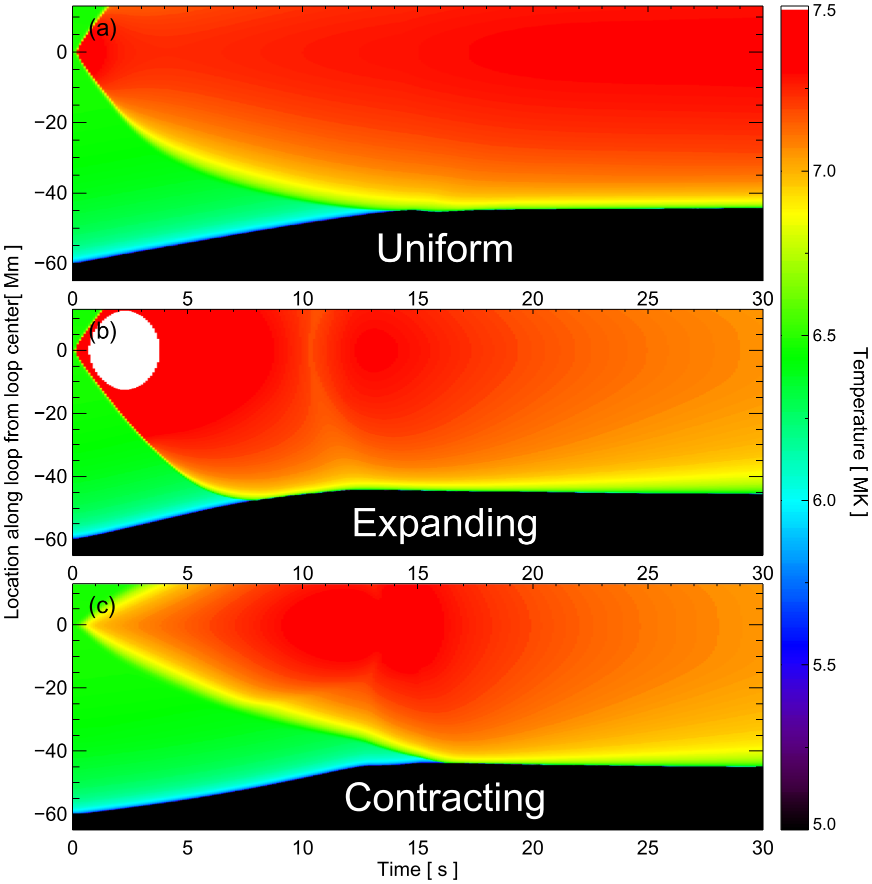

Figure 10. Temperature stack plots for each of the three runs: (a) the uniform case, (b) the expanding case, and (c) the contracting case. Each panel shows the time evolution of the loop temperature from $10^{5.0}$ to $10^{7.5}$ K, as shown by the color bar on the right. Temperatures above $10^{7.5}$ K appear white, and regions outside the flux tube appear black.

primarily affect temperature. The central plug of high density, compressed by the RD-powered jets, appears as a lighter-blue horizontal band near the top at $\ell = 0$. This material is dense and hot and so is accompanied by a rise in central pressure that seeks to expand the plug. At the same time, more material is constantly being added to the central plug by the jets. The result is that while the plug does expand (the horizontal bands are slightly triangular), the central high pressure is preserved even past the end of retraction. Only at later times does the central pressure begin to drive the plug into the surrounding plasma. Confirmation of this can be seen in panel (c) of Figures 6–8 displaying the pressure.

Central plug compression occurs in the expanding case, panel (b), but with a slight complication not found in the uniform case. In the expanding case, the flux tube retracts into weaker field, which increases its cross-sectional area. This means that the inward jets are adding mass to a central region of increasing volume, greatly offsetting any possible density increase. Were the jets absent, the increasing area would drive down the tube's density. This does occur in the legs surrounding the central region, resulting in relative voids that appear as darker-blue regions in Figure 11(b).

The contracting case exhibits behavior opposite to this. The jets add material to a central region whose cross section is diminishing as retraction moves the tube into increasing field, i.e., decreasing volume. The central plug is therefore squeezed from all sides, producing a relatively high density, evident as a horizontal band of lighter shade than either other case. This omnidirectional compression lasts only until the central region has pulled through the maximum field, after which it encounters weakening field. At this point, we see the appearance of relative voids in the areas adjacent to the central region.

Differences in both temperature and density evolution combine to produce differing evolutions of DEM. Spatially integrated, time-resolved DEMs of each run are plotted in Figure 12. The vertical axis of each plot is the logarithm of temperature, the horizontal axis is time, and color represents log (DEM) from blue to red. Four notable features are present in each of the three cases. First is the darkening, or dimming (i.e., blue region), beginning $t = 0$ at roughly $T = 10^{6.5} = 3\,\mathrm{MK}$ and sweeping down to $T = 10^{4.5} = 30{,}000\,\mathrm{K}$. This shows coronal plasma heated from its initial temperatures to tens of MK, leaving a dearth of emission measure in the ranges at and below 3 MK. The dimming sweeps down over time as the thermal conduction front moves to decreasing temperatures in the loop's legs. The progression of this sweep differs slightly between runs according to the rate of heating and speed of the conduction front moving down the legs.

The next important feature is the enhanced emission measure (red and saturated white) in the cooler bands, below $T = 10^{6.0} = 1\,\mathrm{MK}$, after the conduction front has reached the chromosphere. This feature comes about from the increased pressure in the chromosphere, leading to compression at the leading edge of the downward-moving condensation front. This

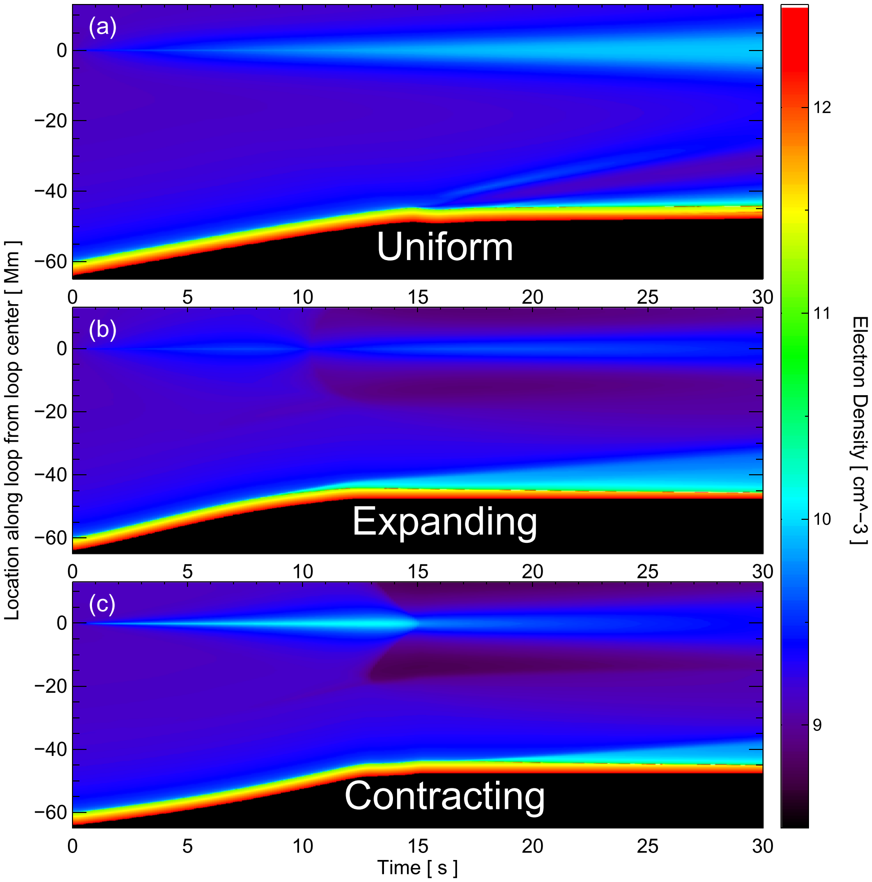

Figure 11. Electron density stack plots for each for (a) the uniform case, (b) the expanding case, and (c) the contracting case. Each panel shows the time evolution of half the loop from $10^{8.5}$ to $10^{12.0}$ cm^{-3} in electron density, as shown by the color bar on the right.

enhancement in DEM at lower temperatures is paired with the third important feature, the enhanced emission in the megakelvin range at roughly the same time. This appears as upward green and orange regions sloping upward and then persisting in time. It reflects the material heated to coronal temperatures by the conduction front—material evaporated into the corona. It is noteworthy that conduction cannot create temperatures exceeding the loop-top source's peak temperature.

The final feature of note is the behavior of the hottest emission. Both the uniform and expanding cases show a "finger" of green at $T \simeq 10^{7.3} = 20\,\mathrm{MK}$ from the beginning ($t = 0$). In the expanding case the upper green edge slopes more gradually upward but persists longer than the other cases. In the uniform case the temperature peaks quickly, but in such a rarefied region that the emission measure of the source is relatively low and dies off rapidly as conduction moves the heat throughout the rest of the tube. The continuing action of the jets, however, piles up material and continues to heat it, and as a result there is a bounce-back with slightly cooler material, but appearing much brighter. The expanding case shows a similar type of behavior. At first the jets produce the peak temperature, and in this case it is bright emission. The thermal energy is quickly spread through the flux tube, and this emission is lost. The continuing action of the jets work to heat the central region, and slightly cooler material brightens in the central plug again. It cools more quickly than in the uniform case. The behavior in the contracting case is, once again, opposite to this. Owing to its more slowly building heat, we see a gradual rise to the peak emission. It then cools like the expanding case and experiences no bounce-back to a slightly cooler bright source.

The differences described above lead to clear and potentially observable differences in time-integrated DEM, plotted in Figures 12(d)–(f). The curves show the integral of the time-resolved DEM immediately to the left, along the same vertical temperature axis. For simpler comparison each DEM is multiplied by a typical reconnection rate of $10^{18}\,\mathrm{Mx\,s^{-1}}$ to get a volumetric DEM of the run as a whole (Jing et al. 2005; Longcope et al. 2010; Kazachenko et al. 2017). Since a flare consists of numerous independently contracting loops, a time-integrated observation will resemble this plot more than a slice of the time-resolved DEM (Longcope et al. 2018). For ready comparison, each panel overplots the integrated DEM from all three cases using the same colors as Figure 4: black for the uniform, red for the expanding, and violet for the contracting case. The curve matching the panel to its left is plotted solid, and the other two dashed. It is immediately clear that the uniform case carries significantly less emission in the megakelvin range for reasons previously discussed. The expanding case has more megakelvin emission than the other two, as a result of the strong conduction front and the aggressive evaporation.

Significantly, the contracting and uniform runs both show DEM peaks in the hottest range, while the expanding case does not. While that run does experience temperatures that high, and even higher, it is brief enough and lacks the density necessary to produce DEM comparable to the other two cases. It is notable that the contracting case produces high temperature

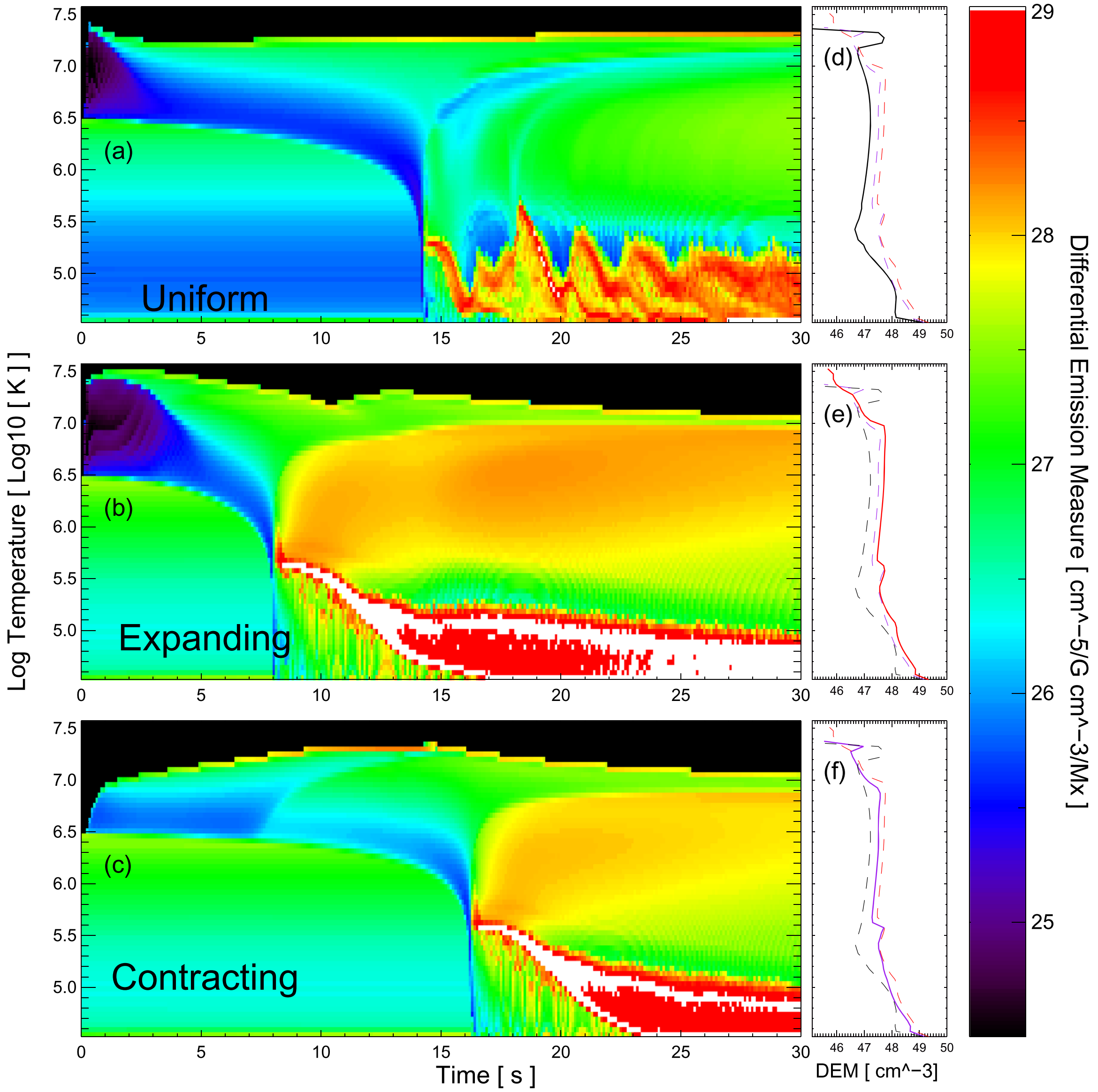

Figure 12. DEMs for (a, d) the uniform case, (b, e) the expanding case, and (c, f) the contracting case. The left column (panels (a)–(c)) shows time-resolved DEMs using a color scale from 10^{24} cm^{-5} G^{-1} (violet) to 10^{29} cm^{-5} G^{-1} (red) against time on the horizontal axis and log(T) on the vertical axis. The right column (panels (d)–(f)) plots as a solid line the time-integrated version of the DEM to its left using the same vertical temperature axis. The other two curves are plotted dashed for reference. The time integral is multiplied by 10^{18} Mx s^{-1} to obtain a full-flare DEM with units of cm^{-3}.

later than the contracting case, but also that it persists longer, thereby producing the observed high-temperature peak.

5. Discussion

The foregoing analysis has shown observable differences arising from reconnection at different locations within different kinds of global current sheets. We investigated three distinct cases: reconnection in a uniform sheet, reconnection above the pinch point, and reconnection at the pinch point. To do so, we created a simple 2.5-dimensional current sheet, from which we then created the two nonuniform reconnection scenarios. Each flux tube was initialized in a similar way, with the current sheet field being the principal difference between cases. The TFT was used to find the post-reconnection time evolution in each case. The most notable difference between the cases was that reconnection above the pinch point, called the contracting case, exhibited a relatively long-lasting, high-density plug of superhot material (i.e., $T \sim 20$ MK). This was evident both in the density plot and as a peak in the time-integrated DEM.

Some observations have found evidence of superhot hard X-ray sources at or above the flare loop top (Kosugi et al. 1994; Veronig et al. 2006; Caspi & Lin 2010). The chief challenge posed by these observations is to enhance the density in a high-temperature plasma. It has been proposed that this can be achieved through the confining parallel jets supplied by the RDs (Longcope et al. 2010, 2016). Here we have found that this parallel compression is augmented by lateral compression in cases where reconnection occurs above the point of peak field strength in the current sheet. In this sense, observations of superhot loop-top sources appear to support that particular site for localized flare reconnection.

Other explanations have been proposed to explain above-the-loops hard X-ray sources. Some observers have invoked a population of nonthermal electrons (Sui et al. 2004) that could not be described using a fluid model like ours. Other models create superhot coronal sources in different ways, such as through successive reconnection as in Karlický & Bárta (2011), fast-mode termination shocks (Aurass et al. 2002; Shen et al. 2018), or instabilities driving complex interactions (Fang et al. 2016). These effects are beyond the scope of our strictly fluid model.

Reconnection under the contracting scenario has been proposed in some previous flare investigations. Longcope et al. (2018) found evidence for it in EUV images of the plasma sheet above the limb flare on 2017 September 10. They used similar TFT simulations, via PREFT, to show that the inflow jets combined with lateral flux tube compression could enhance the density almost 20-fold—just enough to match the observations. Retraction into strengthening field is also invoked as a mechanism for accelerating nonthermal particles in the so-called collapsing trap model (Levine 1974; Somov & Kosugi 1997; Karlický & Kosugi 2004). Particles experience an energy gain scaling with the field strength increase. In the contacting case we modeled the field strength increase was less than 1.5 (from ~40 to 56 G), so we would expect rather modest energy gains at best. But our model neglects nonthermal populations since it is focused exclusively on the bulk plasma dynamics. On the other hand, collapsing trap models often neglect the thermal plasma and almost never include the kinds of self-consistent density and temperature increases that we find will occur within the collapsing trap. A study combining these two elements remains a task for future investigation.

The TFT model provided us an expedient means to explore the differences in reconnection geometry, albeit with some loss of fidelity due to its approximations. Because it treats the post-reconnection evolution in an ideal current sheet, the TFT model includes no electrical resistivity. While some diffusive process is an essential part of the reconnection process, this is thought to play little role in the global exterior region where energy release occurs. It is this nondiffusive, post-reconnection energy release that TFT seeks to model. The TFT tacitly neglects any possible interaction with other reconnected flux or with the plasma around itself. One consequence of this neglect is that reconnected flux retracts at speeds approaching the local Alfvén speed. This is, however, common to many theoretical reconnection models: they generally predict reconnection outflow at Alfvénic speeds (Petschek 1964; Soward 1982). Unfortunately, our theoretical model falls into this same category.

The different cases were affected differently by the profile of the current sheet magnetic field. The timing of each flux tube's retraction differed, with the expanding case being the fastest as it was pushed downward by magnetic pressure. As the retraction converted magnetic energy into heat through jets and viscous interactions, the expanding case experienced the highest temperature, while the contracting case had the lowest, due to its low conversion rate. The difference in temperature led to the difference in the thermal conduction front, with the expanding case having the fastest moving front. The magnetic field also changed the density of each run by compressing or expanding each tube. The contracting case experienced the highest density as the field squeezed the tube while the jets piled in material.

To illustrate the observable consequences, we constructed time-resolved and time-integrated DEMs for each tube over the duration of the simulation. Each run showed similar features, but with different emphasis as a result of the different dynamics. While the expanding run showed the highest temperatures, it did so in relatively rarefied material that produced low emission. The contracting run, on the other hand, reached its peak temperature when it had accumulated a plug of dense material, leading to higher emission measure. Overall the expanding run did not show sustained emission in tens of megakelvin ranges, where we consistently see emission in the extreme-ultraviolet. The other two cases, despite lower temperatures, did produce a peak in emission in the same range.

An expanding flux tube type scenario generates peak heat up front when it does not have a large density and results in emission dropping off in the higher temperatures. This contrasts with the contracting and uniform cases that both show an excess of emission at the higher temperatures instead of decreasing smoothly. While increasing the field strength or increasing the energy release may shift the peak around, or shift the decay in emissions higher, it is unlikely to change the result of the DEM. In the future, we would like to expand on this work by considering a more varied parameter space to verify that this relationship holds for more varied current sheets.

This work was supported partly by grant NNX16AH04G from NASA's Heliophysics Supporting Research (HSR) program.

ORCID iDs

John Unverferth https://orcid.org/0000-0002-7983-3851

References

Aly, J. J., & Amari, T. 1989, A&A, 221, 287
Aurass, H., Vršnak, B., & Mann, G. 2002, A&A, 384, 273
Baty, H., Priest, E. R., & Forbes, T. G. 2006, PhPl, 13, 022312
Bhattacharjee, A., Huang, Y.-M., Yang, H., & Rogers, B. 2009, PhPl, 16, 112102
Biernat, H. K., Heyn, M. F., & Semenov, V. S. 1987, JGR, 92, 3392
Birn, J., Drake, J. F., Shay, M. A., et al. 2001, JGR, 106, 3715
Biskamp, D., & Schwarz, E. 2001, PhPl, 8, 4729
Braginskii, S. I. 1965, in Reviews of Plasma Physics, ed. M. A. Leontovich (New York: Consultants Bureau), 205
Caspi, A., & Lin, R. P. 2010, ApJL, 725, L161
Drake, J. F., Cassak, P. A., Shay, M. A., Swisdak, M., & Quataert, E. 2009, ApJL, 700, L16
Erkaev, N. V., Semenov, V. S., & Jamitsky, F. 2000, PhRvL, 84, 1455
Fang, X., Yuan, D., Xia, C., Van Doorsselaere, T., & Keppens, R. 2016, ApJ, 833, 36
Forbes, T. G., & Priest, E. R. 1987, RvGeo, 25, 1583
Forbes, T. G., Priest, E. R., Seaton, D. B., & Litvinenko, Y. E. 2013, PhPl, 20, 052902
Forbes, T. G., Seaton, D. B., & Reeves, K. K. 2018, ApJ, 858, 70
Green, R. M. 1965, in IAU Symp. 22, Stellar and Solar Magnetic Fields, ed. R. Lust (Amsterdam: North Holland), 398
Guidoni, S. E., & Longcope, D. W. 2011, ApJ, 730, 90
Hesse, M., Schindler, K., Birn, J., & Kuznetsova, M. 1999, PhPl, 6, 1781
Jing, J., Qiu, J., Lin, J., et al. 2005, ApJ, 620, 1085
Karimabadi, H., Krauss-Varban, D., Huba, J. D., & Vu, H. X. 2004, JGR, 109, A09205
Karlický, M., & Bárta, M. 2011, ApJ, 733, 107
Karlický, M., & Kosugi, T. 2004, A&A, 419, 1159
Kazachenko, M. D., Lynch, B. J., Welsch, B. T., & Sun, X. 2017, ApJ, 845, 49
Kosugi, T., Sakao, T., Masuda, S., et al. 1994, in Proc. Kofu Symp. 127, 127
Landi, S., Del Zanna, L., Papini, E., Pucci, F., & Velli, M. 2015, ApJ, 806, 131
Levine, R. H. 1974, ApJ, 190, 457
Linton, M. G., & Longcope, D. W. 2006, ApJ, 642, 1177
Longcope, D., Unverferth, J., Klein, C., McCarthy, M., & Priest, E. 2018, ApJ, 868, 148
Longcope, D. W. 2014, ApJ, 795, 10

Longcope, D. W., Des Jardins, A. C., Carranza-Fulmer, T., & Qiu, J. 2010, SoPh, 267, 107

Longcope, D. W., & Forbes, T. G. 2014, SoPh, 6, 2091

Longcope, D. W., Guidoni, S. E., & Linton, M. G. 2009, ApJL, 690, L18

Longcope, D. W., & Klimchuk, J. A. 2015, ApJ, 813, 131

Longcope, D. W., Qiu, J., & Brewer, J. 2016, ApJ, 833, 211

MacNeice, P., Burgess, A., McWhirter, R. W. P., & Spicer, D. S. 1984, SoPh, 90, 357

Petschek, H. E. 1964, in AAS-NASA Symp. The Physics of Solar Flares, ed. W. N. Hess (Washington, DC: NASA), 425

Priest, E. R., & Raadu, M. A. 1975, SoPh, 43, 177

Pritchett, P. L., & Coroniti, F. V. 2004, JGR, 109, 1220

Rosner, R., Tucker, W. H., & Vaiana, G. S. 1978, ApJ, 220, 643

Shay, M. A., Drake, J. F., & Swisdak, M. 2007, PhRvL, 99, 155002

Shen, C., Kong, X., Guo, F., Raymond, J. C., & Chen, B. 2018, ApJ, 869, 116

Somov, B. V., & Kosugi, T. 1997, ApJ, 485, 859

Soward, A. M. 1982, JPlPh, 28, 415

Spruit, H. C. 1981, A&A, 98, 155

Sui, L., Holman, G. D., & Dennis, B. R. 2004, ApJ, 612, 546

Syrovatskiĭ, S. I. 1971, JETP, 33, 933

Vasyliunas, V. M. 1975, RvGSP, 13, 303

Veronig, A. M., Karlický, M., Vršnak, B., et al. 2006, A&A, 446, 675

Yokoyama, T., & Shibata, K. 1994, ApJL, 436, L197